A Method for Material Classification in AVIRIS Data with Unknown Atmospheric and Geometric Parameters

David Slater and Glenn Healey
Computer Vision Laboratory
Electrical and Computer Engineering
University of California
Irvine, CA 92697
dslater,healey@ece.uci.edu

Abstract

The measured spectral radiance signature for a material can vary significantly due to atmospheric conditions and scene geometry. We show using a statistical analysis of a comprehensive physical model that the variation in a material's spectral signature lies in a low-dimensional space. The spectral radiance model includes reflected solar and scattered radiation as well as the effects of atmospheric gases and aerosols. The MODTRAN 3.5 code was employed for computing radiative transfer aspects of the model. Using the new model, we develop a maximum likelihood algorithm for material classification which is invariant to atmospheric conditions and scene geometry. The algorithm is demonstrated for material classification in AVIRIS data.

1 Introduction

The development of airborne hyperspectral imaging spectrometers has provided an important tool for studying the distribution of materials on the surface of the earth. Two such sensors, the Hyperspectral Digital Imagery Collection Experiment (HYDICE) [1] and the Airborne Visible/Infrared Imaging Spectrometer (AVIRIS) [7], obtain over two hundred spectral measurements per spatial location over the spectral range 0.4μm-2.5μm. One goal of these sensors is to provide a spectrum at each spatial location which can be used to recognize the imaged materials. Unfortunately, the sensor radiance measurements are affected by the atmospheric and geometric conditions under which they were obtained. In order to extract intrinsic surface properties, atmospheric and geometric effects must be accounted for. Some methods for atmospheric correction are based on knowledge about the spectral reflectance of surfaces on the ground [3] [6]. Another approach [8] is to measure downwelling irradiance on the ground to factor out atmospheric effects. Neither of these approaches is feasible for fully automated material classification.

In this paper, we analyze the effects of atmospheric and geometric factors on the 0.4μm-2.5μm radiance spectra measured by an airborne imaging spectrometer. We begin by presenting

a model for image spectral irradiance. Using this model and the MODTRAN 3.5 atmospheric modeling program [2] we generate a set of spectra which span the range of atmospheric and geometric conditions. We show that these spectra are accurately represented by a low-dimensional linear model. We use this model to derive a maximum likelihood approach to material classification which is invariant to atmospheric and geometric conditions.

2 Modeling Radiance Spectra

Consider a surface with normal $\overline{n}$ on the ground at elevation z_g with an associated coordinate system defined by polar angle θ and azimuthal angle ϕ. The surface is viewed by a sensor at elevation z from direction (θ_v, ϕ_v) and the solar direction is (θ_o, ϕ_o) as shown in figure 1. The spectral radiance incident upon sensor location (x, y) is given by

$$\begin{aligned}\rho(x,y,\lambda) &= T_u(z_g,z,\theta_v,\phi_v,\lambda)R(x,y,\lambda)[KT_d(z_g,\theta_o,\phi_o,\lambda)E_o(\lambda)cos(\theta_o) \\ &\quad + \int_{\phi=0}^{2\pi}\int_{\theta=0}^{\frac{\pi}{2}} E_s(\theta,\phi,\lambda)cos(\theta)sin(\theta)d\theta d\phi] + P(z_g,z,\theta_v,\phi_v,\lambda) \qquad (1)\end{aligned}$$

where $T_u(z_g, z, \theta_v, \phi_v, \lambda)$ is the upward atmospheric transmittance, $R(x, y, \lambda)$ is the spectral reflectance of the matte surface projecting to sensor location (x, y), K is a binary constant which accounts for occluding bodies in the solar to surface path, $T_d(z_g, \theta_o, \phi_o, \lambda)$ is the downward atmospheric transmittance, $E_o(\lambda)$ is the extraterrestrial solar radiance, $E_s(\theta, \phi, \lambda)$ is the scattered sky radiance (i.e. excluding direct solar radiance) per unit solid angle incident on the surface from direction (θ, ϕ), $P(z_g, z, \theta_v, \phi_v, \lambda)$ is the path scattered radiance, and λ denotes wavelength. Thus, the three primary contributors to the observed spectral radiance $\rho(x, y, \lambda)$ for a surface are due to reflected solar illumination, reflected sky illumination, and path radiance. To illustrate the wide variability of radiance spectra, figure 2 is a plot of two calculated radiance spectra for a white matte surface under two different atmospheric and geometric configurations.

3 Signature Dimensionality Analysis

3.1 Physical Background

The atmosphere is a heterogeneous mixture of many gases and aerosols, several of which interact with electromagnetic energy in the visible and near infrared through scattering and absorption as modeled in equation (1) by $T_u(z_g, z, \theta_v, \phi_v, \lambda)$ and $T_d(z_g, \theta_o, \phi_o, \lambda)$. In order to interpret accurately measured spectra, it is necessary to account for the effects of these attenuating constituents. Moreover, spatial and temporal variation in the concentration of atmospheric components makes it impossible to derive a single atmospheric correction function which will work in all circumstances.

Scene geometry also plays an important role in the observed radiance spectrum. From (1), path scattered radiance and atmospheric transmittance depend on sensor and surface altitude.

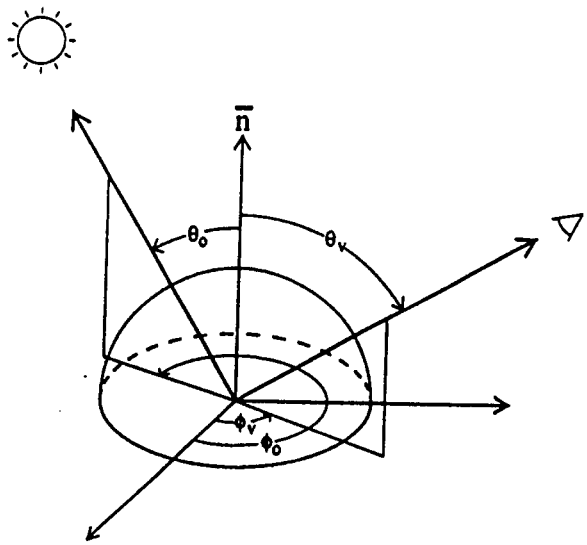

Figure 1: Surface, sensor, solar geometry

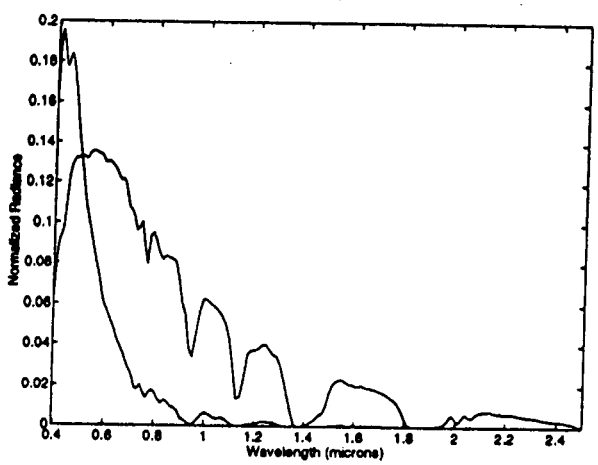

Figure 2: Radiance spectra of a uniform reflecting surface under two different conditions

Solar zenith angle also has a strong influence on the downward atmospheric transmittance because atmospheric path length increases with increasing zenith angle. In addition, nonuniformly distributed occluding bodies such as clouds can block direct solar radiation.

3.2 Linear Models for $L_i(\lambda)$

In this section, we analyze the dimensionality of spectral signatures induced by atmospheric and geometric effects. We rewrite equation (1) as

$$\rho_i(\lambda) = L_i(\lambda)R(\lambda) + P_i(\lambda) \tag{2}$$

where the spatial coordinates have been dropped and the subscript i denotes a particular set of atmospheric and geometric conditions. Note that $L_i(\lambda)$ and $P_i(\lambda)$ depend on atmospheric and geometric properties, but not on surface properties. In addition, for relatively clear conditions, $P_i(\lambda)$ accounts for less than 10% of the total radiance measured by a sensor [3] motivating us to focus on $L_i(\lambda)$ in the following analysis.

Judd *et al.* [5] showed empirically that the spectral distribution of daylight over the visible wavelengths can be well approximated by a linear combination of a small number of basis functions. We apply a similar approach using the physical model in (1) to approximating $L_i(\lambda)$ over 0.4μm - 2.5μm using

$$L_i(\lambda) \approx \sum_{j=1}^{N} \sigma_{ij} l_j(\lambda) \tag{3}$$

where the functions $l_j(\lambda)$ define a fixed basis and the constants σ_{ij} are weighting coefficients.

For a discrete function $L_i(\lambda)$ which is sampled at W wavelengths, define the quality of the approximation in (3) by the squared error

$$E_i = \sum_{k=1}^{W} \left(L_i(\lambda_k) - \sum_{j=1}^{N} \sigma_{ij} l_j(\lambda_k) \right)^2 \tag{4}$$

For a set $L_1(\lambda), L_2(\lambda), \ldots, L_M(\lambda)$ of discrete functions corresponding to different atmospheric and geometric conditions, the total squared error associated with a set of basis functions is

$$E_T = \sum_{i=1}^{M} E_i \tag{5}$$

Consider a $W \times M$ matrix X with each column containing a discrete function $L_i(\lambda)$. We can compute an orthonormal basis for the column space of X using the singular value decomposition [4]

$$X = U\Sigma V^T \tag{6}$$

For any N, the first N columns of U provide an orthonormal basis set $l_1(\lambda), l_2(\lambda), \ldots, l_N(\lambda)$ which minimizes E_T.

Scene Parameter	Values
H_2O (cm)	0.39, 0.88, 1.44, 2.14, 3.11, 4.33
O_3 (atm cm)	0.07, 0.11, 0.12, 0.14, 0.15
O_2 (atm m)	8407.9, 8604.0, 9179.4, 9453.2, 10536.8, 11713.4
CH_4 (atm cm)	0.83, 0.84, 0.85, 0.86, 0.87
NO (atm cm)	0.0001, 0.0002
N_2O (atm cm)	0.189, 0.199, 0.202, 0.209, 0.214, 0.221
CO (atm cm)	0.064, 0.065, 0.066, 0.067, 0.070, 0.072
CO_2 (atm m)	15.24, 16.61, 17.63, 17.82, 18.92, 19.36
Solar-zenith angle	5°, 15°, 25°, 35°, 45°, 55°, 65°, 75°
Aerosol type	rural, urban, maritime, desert
Visibility (km)	5, 23, 50, 70, 85, 100
Sensor Altitude (km)	0, 1, 2, 3, 4, 5, 6

Table 1: Range of atmospheric and geometric parameters for linear model computation

An important question is how many $l_j(\lambda)$ basis functions are required to approximate accurately a large set of $L_i(\lambda)$ functions corresponding to different atmospheric and geometric conditions. The first step is to construct a representative set of $L_i(\lambda)$ functions. We generated such a set using (1) and MODTRAN 3.5. The set consisted of 4032 functions spanning the range of atmospheric and geometric parameters listed in Table 1. These functions were then used to compute $l_j(\lambda)$ using (6). Figure 3 is a plot of $\frac{E_T}{M}$ as a function of N for the 4032 spectra database. Note that $\frac{E_T}{M}$ is small when $N = 5$.

4 Invariant Recognition

In this section, we describe an approach to recognizing materials having a known spectral reflectance function $R(\lambda)$ under unknown outdoor conditions. Using a discrete form of (2), a multispectral sensor obtains a vector of W measurements at each spatial location given by

$$\rho(\lambda_i) = L(\lambda_i)R(\lambda_i) + \eta(\lambda_i) \qquad 1 \leq i \leq W \tag{7}$$

where $\eta(\lambda_i)$ is zero mean gaussian noise for the ith band and we neglect path radiance. If the elements $L(\lambda_i)$ are represented by

$$L(\lambda_i) = \sum_{j=1}^{N} \sigma_j l_j(\lambda_i) \qquad 1 \leq i \leq W \tag{8}$$

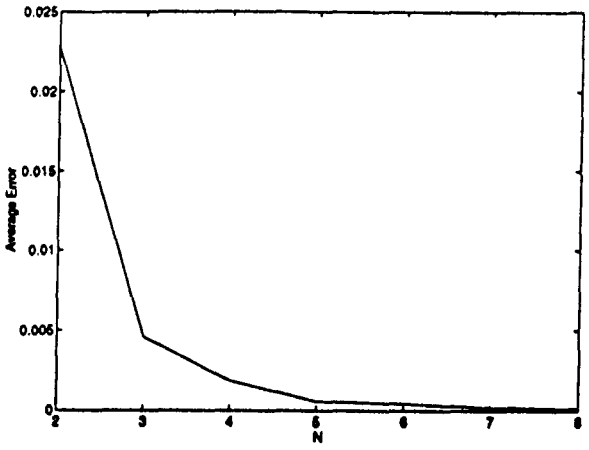

Figure 3: Error for linear model

as in (3), then (7) can be written

$$\rho(\lambda_i) = \sum_{j=1}^{N} \sigma_j v_j(\lambda_i) + \eta(\lambda_i) \qquad 1 \leq i \leq W \tag{9}$$

where $v_j(\lambda_i) = R(\lambda_i) l_j(\lambda_i)$. Let ρ, v_j, R, and η be W-dimensional column vectors composed of elements from $\rho(\lambda_i)$, $v_j(\lambda_i)$, $R(\lambda_i)$, and $\eta(\lambda_i)$ for $1 \leq i \leq W$. The conditional probability of measuring sensor vector ρ for a material with spectral reflectance vector R is

$$P(\rho|R) = \frac{1}{(2\pi)^{0.5W}|\Sigma|^{0.5}} \exp\left(-0.5 D^T \Sigma^{-1} D\right) \tag{10}$$

where Σ is the covariance matrix of the noise vector η and

$$D = \rho - \sum_{j=1}^{N} \sigma_j v_j \tag{11}$$

From (10), maximum likelihood estimates for the parameters $\sigma_1, \sigma_2, \ldots, \sigma_N$ can be obtained by differentiating $D^T \Sigma^{-1} D$ with respect to $\sigma_1, \sigma_2, \ldots, \sigma_N$ and setting each of the N equations to 0. The estimated parameters can be substituted into (10) to obtain the likelihood of the measurement vector ρ for a material with reflectance vector R. This likelihood can be computed at each spatial location in the image and thresholded for illumination-invariant material classification.

5 Experimental Verification

To verify the applicability of the linear model to real data, we examined several measured spectra. The spectra were obtained under relatively clear conditions so that the path scattered

radiance $P_i(\lambda)$ is small. Thus, we determine $L_i(\lambda)$ by

$$L_i(\lambda) = \frac{\rho_i(\lambda)}{R(\lambda)} \tag{12}$$

using available spectral reflectance data $R(\lambda)$. We fit several of these measured $L_i(\lambda)$ functions using the linear model computed in section 3. Each side of figure 4 is a plot of $L_i(\lambda)$ and the corresponding fit using 5 basis functions. We see that although the spectra were obtained under different conditions, the five dimensional model is quite accurate for each case. As an additional test of the model, we classified surface materials in the Cuprite, Nevada AVIRIS [7] images shown in figures 5(a) and 6(a) using the method in section 4 in conjunction with spectral reflectance data obtained from the USGS Spectroscopy Laboratory. The complex three dimensional geometry of the Cuprite scene requires an illumination-invariant classification approach because ground orientation, as well as the presence of shadowing surfaces such as mountains, affects the spectral distribution of illumination falling on surface materials. Both sides of Figure 4, in fact, are $L_i(\lambda)$ functions incident on the same material at different locations in these scenes. Figures 5(b) and 6(b) show the results of classification. The white areas in figures 5(b) and 6(b) are Alunite, the light gray areas are Kaolinite, and the dark gray areas are a mixture of Alunite and Silica. Figure 7(a) is a plot of a measured radiance spectrum of Alunite with its corresponding fit, figure 7(b) is a plot of a measured radiance spectrum of an Alunite/Silica mixture with its corresponding fit, and figure 8 is a plot of a measured radiance spectrum of Kaolinite with its corresponding fit. The classification results are in strong agreement with the mineral distribution in the region.

6 Summary

In this paper, we examined the effects of variations in the atmospheric conditions and scene geometry on outdoor illumination functions. Using a physical model, we generated spectra which enumerate a large range of conditions. The calculated spectra were used to compute a linear model for the space of atmospheric and geometric variation. We showed that a five parameter linear model is adequate to represent the gamut of atmospheric and geometric effects. This model can be used for automated material classification invariant to atmospheric conditions and scene geometry. We verified the accuracy of the linear model using several measured spectra corresponding to ground regions with known spectral reflectance.

References

[1] R. W. Basedow, D. C. Armer, and M. E. Anderson. HYDICE system: Implementation and performance. In *SPIE Proceedings*, volume 2480, pages 258-267, 1995.

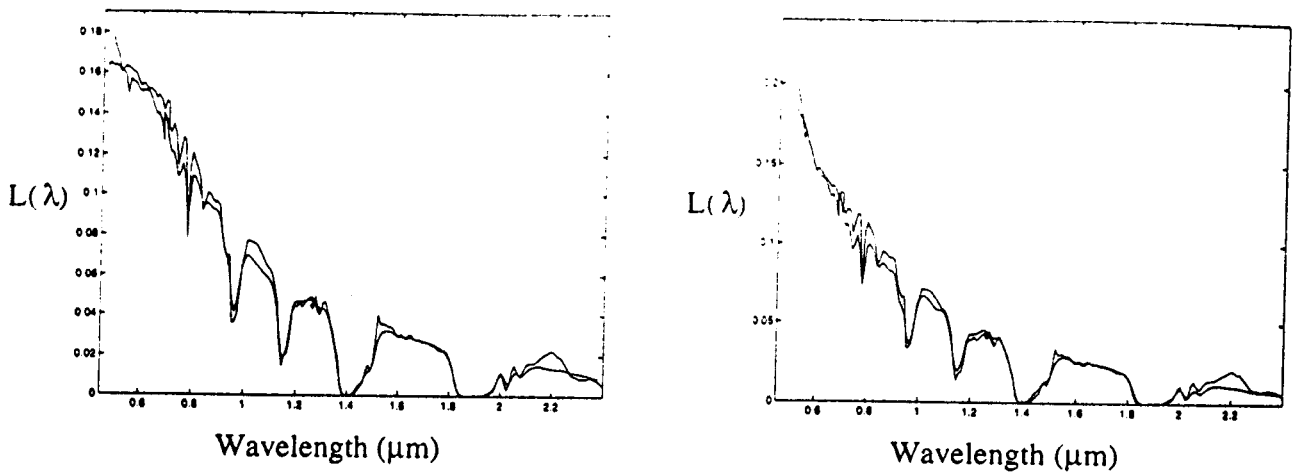

Figure 4: Measured spectra and fits

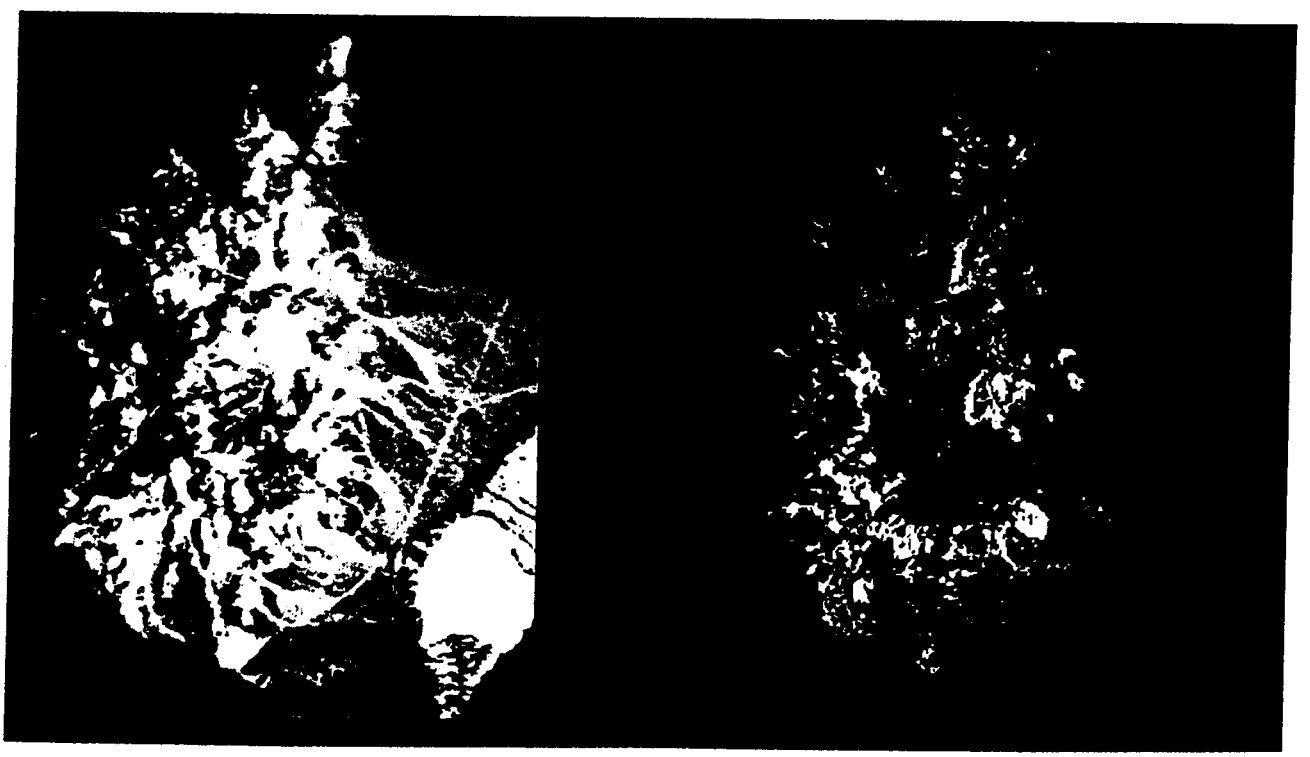

Figure 5: (a) AVIRIS image 1 of Cuprite, Nevada. (b) Classification results for AVIRIS image 1.

Figure 6: (a) AVIRIS image 2 of Cuprite, Nevada. (b) Classification results for AVIRIS image 2.

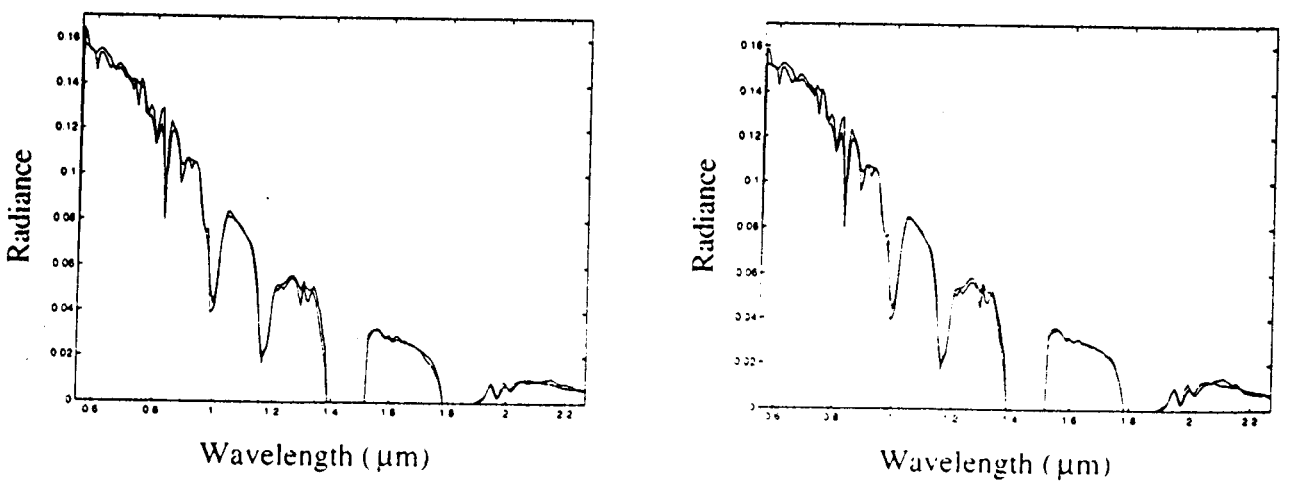

Figure 7: (a)Measured Alunite radiance and fit. (b) Measured Alunite/Silica mixture radiance and fit.

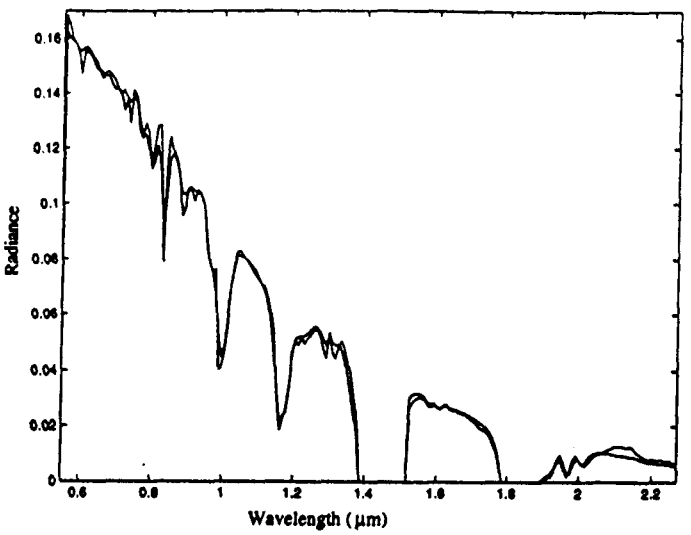

Figure 8: Measured Kaolinite radiance and fit

[2] A. Berk, L. S. Bernstein, and D. C. Robertson. MODTRAN: a moderate resolution model for LOWTRAN 7. Technical Report GL-TR-89-0122, Geophysics Laboratory, Bedford, Massachusetts, 1989.

[3] B. C. Gao and A. F. H. Goetz. Column atmospheric water vapor and vegetation liquid water retrievals from airborne imaging spectrometer data. *Journal of Geophysical Research*, 95(D4):3549–3564, 1990.

[4] G.H. Golub and C.F. van Loan. *Matrix Computations*. Johns Hopkins University Press, Baltimore, MD, 1983.

[5] D. B. Judd, D. L. MacAdam, and G. Wyszecki. Spectral distribution of typical daylight as a function of correlated color temperature. *Journal of the Optical Society of America*, 54(8):1031–1040, 1964.

[6] R. Richter. Correction of atmospheric and topographic effects for high spatial resolution satellite imagery. In *Proceedings of the SPIE, Algorithms for Multispectral and Hyperspectral Imagery III*, pages 216–224, Orlando, Florida, 1997.

[7] G. Vane, R. O. Green, T. G. Chrien, H. T. Enmark, E. G. Hansen, and W. M. Porter. The airborne visible/infrared imaging spectrometer (AVIRIS). *Remote Sensing of the Environment*, 44:127–143, 1993.

[8] D. J. Williams, A. Royer, N. T. O'Neill, S. Achal, and G. Weale. Reflectance extraction from CASI spectra using radiative transfer simulations and a rooftop irradiance collector. *Remote Sensing of the Environment*, 44:165–178, 1993.